Inorganic Chemistry

Article

pubs.acs.org/IC

Phosphorescent Zinc Probe for Reversible Turn-On Detection with Bathochromically Shifted Emission

Seung Yeon Ryu,[†] Mijoung Huh,[†] Youngmin You,[*,‡] and Wonwoo Nam[*,†]

[†]Department of Chemistry and Nano Science and [‡]Division of Chemical Engineering and Materials Science, Ewha Womans University, Seoul 120-750, Korea

Supporting Information

ABSTRACT: Phosphorescent molecules are attractive complements to fluorescent compounds for bioimaging. Time-gated acquisition of the long-lived phosphorescence signals provides an effective means to eliminate unwanted background noises due to short-lived autofluorescence. We have previously investigated the molecular principles governing modulation of photoinduced electron transfer in phosphorescence zinc probes that were based on biscyclometalated Ir(III) complexes (Woo, H. et al. *J. Am. Chem. Soc.* **2013**, 135, 4771−4787). The studies established that phosphorescence turn-on responses would be attainable for Ir(III) complexes with high triplet-state energies. This sets an upper limit to an emission wavelength, restricting the development of red- or near-IR-phosphorescence turn-on probes. To address this challenge, we designed and synthesized a new phosphorescent probe having an electron-deficient 2-(2-pyridyl)pyrazine diimine ligand tethering a di(2-picolyl)amine (DPA) zinc receptor. This ligand control led to red phosphorescence emission (λ_{ems} = 596 nm), with an excited-state reduction potential (E^*_{red}) retained as high as 1.44 V versus standard calomel electrode (SCE). The E^*_{red} value was more positive than the ground-state oxidation potential of DPA (1.05 V vs SCE), permitting an occurrence of photoinduced electron transfer at a rate of 2×10^7 s^{-1}. Zinc binding at DPA abolished the electron transfer to produce phosphorescence turn-on signaling. The probe was capable of detecting zinc ions selectively over other competing biological metal ions in aqueous buffer solutions (pH 7.4, 20 mM piperazine-*N*,*N*′-bis(2-ethanesulfonic aid)) with the zinc dissociation constant of 109 pM. Finally, bioimaging utility of the probe has been successfully demonstrated by visualizing exogenously supplied zinc ions in live HeLa cells. The research described in this paper demonstrates that judicious ligand control enables retention of turn-on responses in the low-energy phosphorescence region.

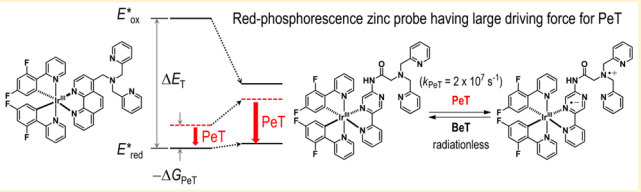

I. INTRODUCTION

Phosphorescence modality offers unique advantages in bioimaging, as the long-lived emission facilitates utilization of time domains.[1−3] Among the various classes of phosphorescent molecules, cyclometalated Ir(III) complexes have been most successful for bioimaging purposes.[4−16] In particular, a range of phosphorescent sensors that reversibly report the spatiotemporal fluctuations of biometals have been developed.[3,17−21] Photoinduced electron transfer (PeT) is utilized to create the metal ion probes, because the nonradiative PeT is several orders faster than phosphorescence transition.[22−29] Metal ion binding abolishes the PeT, restoring phosphorescence emission. We investigated the effectiveness of PeT for creation of phosphorescence zinc probes, based on biscyclometalated Ir(III) complexes and a di(2-picolyl)amino (DPA) zinc receptor.[1,2,30] The studies established that PeT from DPA to the Ir(III) complexes adhered to the Rehm−Weller behavior with $-\Delta G_{PeT} = e\cdot[E_{ox}(DPA) - E^*_{red}(Ir)] + w_p$ ($-\Delta G_{PeT}$, driving force for PeT; e, elementary charge; E_{ox}, the ground-state oxidation potential, w_p, the ion-pairing term; $E^*_{red} = E_{red} + \Delta E_T$, where E_{red} and ΔE_T are the ground-state reduction potential and the triplet-state energy, respectively).[24] Further mechanistic studies revealed that the PeT was located in the Marcus-normal region of electron transfer. On the basis of these findings, it has been predicted that phosphorescence emission of Ir(III) complexes with small ΔE_T cannot be affected by PeT (Scheme 1a). Indeed, we observed the absence of PeT for Ir(III) complexes exhibiting phosphorescence emission at peak wavelengths longer than 517 nm (i.e., $-\Delta G_{PeT} < 0$ when $\Delta E_T < 2.4$ eV).[1] This lower bound of ΔE_T is obviously greater than the case for PeT in fluorescence probes. This thermodynamic loss is ascribed to exchange energy (ΔE_{ST}) existing between singlet excited state (S_1) and triplet state (T_1) (Scheme 1b).

There are two potential approaches to address the challenge: One is to increase the E^*_{red} value of an Ir(III) complex, and the other is to decrease the E_{ox} value of a receptor. In the case of the former approach, the modulation of E^*_{red} should rely on control over E_{red} rather than ΔE_T to keep the emission in the long-wavelength regions. We envisioned that such control could be accomplished by incorporating an electron-deficient diimine (N^N) ligand into biscyclometalated Ir(III) complexes.

Received: April 29, 2015
Published: October 5, 2015

DOI: 10.1021/acs.inorgchem.5b00967
Inorg. Chem. 2015, 54, 9704−9714

Scheme 1[a]

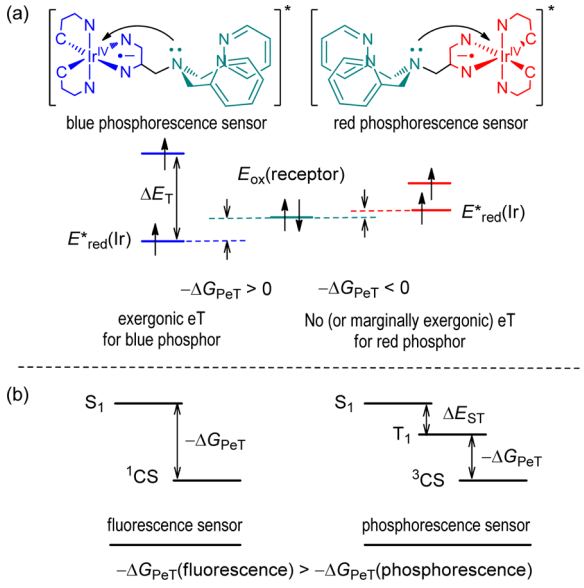

[a](a) The driving force for photoinduced electron transfer ($-\Delta G_{PeT}$) in blue- and red-phosphorescence sensors. (b) Comparison of $-\Delta G_{PeT}$ in a fluorescence sensor and a phosphorescence sensor. ^{1}CS, singlet charge-separated species; ^{3}CS, triplet charge-separated species.

To validate this hypothesis, we chose to employ 2-(2-pyridyl)pyrazine for the N^N ligand. The DPA zinc receptor was introduced to the N^N ligand through an amide linkage.[31,32] We found that this ligand control indeed enabled red phosphorescence emission with a large E^*_{red} value (1.44 V vs standard calomel electrode (SCE)). Herein, we report the design, synthesis, characterizations, and bioimaging applications of a novel phosphorescence zinc probe (ZIrdap in Scheme 2). The sensor produced zinc-induced phosphorescence turn-on responses in the red-emission regions (λ_{ems} = 596 nm) in aqueous buffer solutions (pH 7.4, 20 mM piperazine-*N*,*N*′-bis(2-ethanesulfonic acid) (PIPES)). Spectroscopic and electrochemical investigations revealed the occurrence of exoergic PeT ($-\Delta G_{PeT}$ = 0.39 eV), which was reversibly modulated by zinc binding. Finally, bioimaging utility of the probe was successfully demonstrated by phosphorescence visualization of exogenously supplied zinc ions in live HeLa cells.

II. RESULTS AND DISCUSSION

Synthesis of the Phosphorescence Zinc Sensor. The synthetic route to the phosphorescence zinc sensor (ZIrdap) is depicted in Scheme 2. The Pd(0)-catalyzed Stille reaction between 5-amino-2-bromopyrazine and 2-(tributylstannyl)-pyridine yielded the N^N ligand scaffold. Amidation of the primary amine in the N^N ligand with α-bromoacetyl bromide, followed by substitution of the α-bromide with di(2-picolyl)-amine, yielded the DPA-appended N^N ligand (dap ligand, hereafter). Finally, chelation of the dap ligand to the bis-cyclometalated Ir(III) core produced the desired complex in an overall 16% yield. Spectroscopic characterization data obtained using multinuclear NMR spectroscopy and high-resolution mass spectrometry were fully consistent with the proposed structure. Reference complexes devoid of DPA and the amido DPA moiety were also synthesized to investigate the origin of the phosphorescence zinc responses (Irp and Irap; see Scheme 2 for the structures). Synthetic details and spectroscopic identification data are summarized in the Experimental Section.

Scheme 2. Synthesis of the Phosphorescent Zinc Sensor (ZIrdap) and Its Reference Compounds (Irp and Irap)

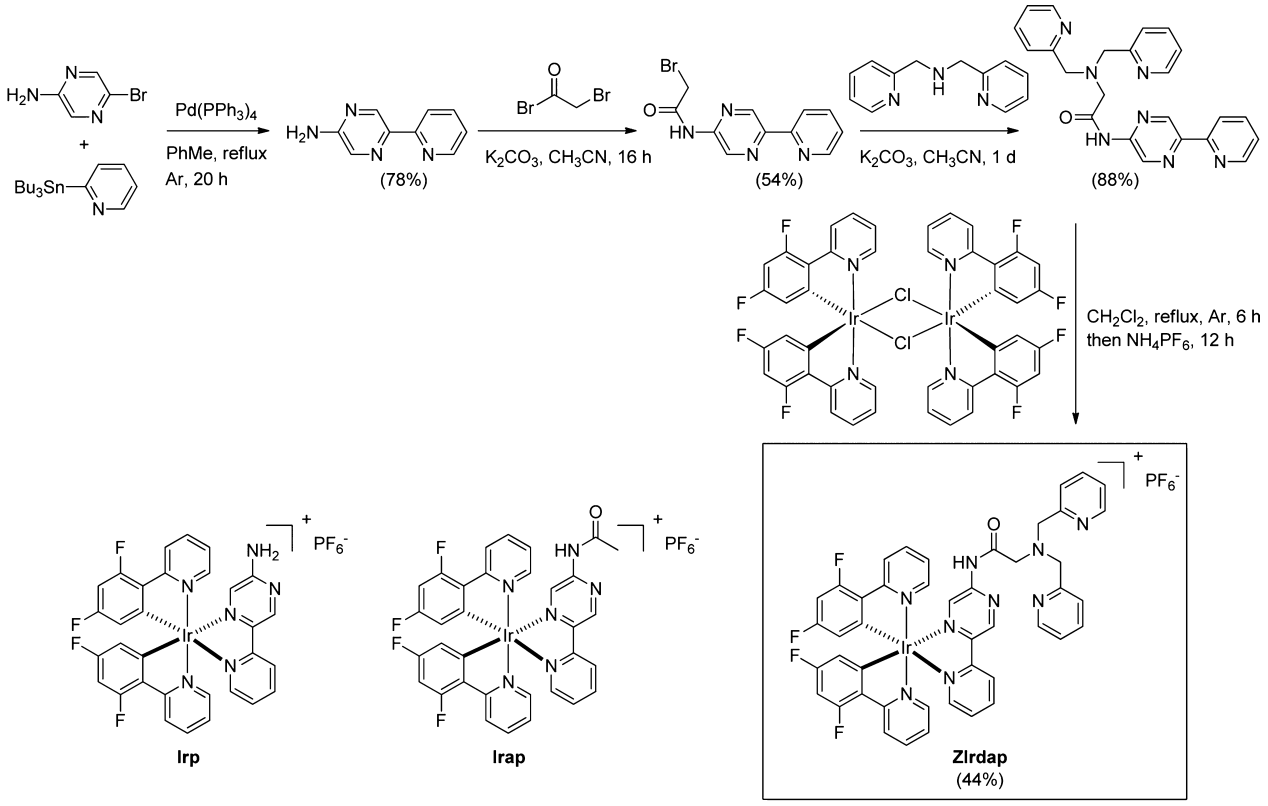

DOI: 10.1021/acs.inorgchem.5b00967
Inorg. Chem. 2015, 54, 9704−9714

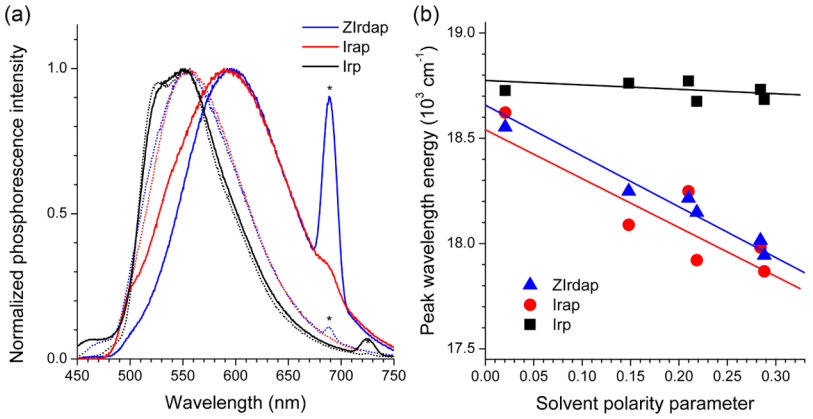

Figure 1. (a) Phosphorescence spectra (dotted lines, CH_3CN; solid lines, aqueous 20 mM PIPES solution at pH 7.4) of 10 μM zinc sensor (ZIrdap) and its reference compounds (Irap and Irp) in the absence of zinc ion. Photoexcitation wavelength = 345 nm (ZIrdap and Irap) and 363 nm (Irp). The asterisks (*) indicate peaks resulting from the second harmonic of the excitation beams. (b) The Lippert−Mataga plot of the phosphorescence peak wavelengths of 10 μM ZIrdap, 10 μM Irap, and 10 μM Irp as a function of the solvent polarity parameter ($f = (\varepsilon - 1)/(2\varepsilon + 1) - (n^2 - 1)/(2n^2 + 1)$; ε and n are the dielectric constant and refractive index of a solvent, respectively).

Mechanism for Phosphorescence Responses of the Zinc Sensor. UV−vis absorption spectra of ZIrdap and its reference compounds carry the bands characteristic of bis-cyclometalated Ir(III) complexes (Supporting Information, Figure S1).[1,33] ZIrdap (10 μM) exhibits orange phosphorescence in acetonitrile solutions with a peak emission wavelength (λ_{ems}) at 554 nm under photoexcitation at 345 nm (Figure 1a). Phosphorescence peak wavelengths of the two reference compounds are found in the similar region (555 and 551 nm for Irap and Irp, respectively), while Irp possesses pronounced vibronic structures. Of particular interest is the bathochromic shifts of the phosphorescence spectra of ZIrdap (λ_{ems} = 596 nm) and Irap (λ_{ems} = 591 nm) in aqueous buffer solutions (20 mM PIPES, pH 7.4). Such a shift is not observed for Irp. As shown in Figure 1b, Lippert−Mataga plots of the phosphorescence peak wavelength energies as a function of the solvent polarity parameter demonstrate the strong positive solvatochromism for ZIrdap and Irap.[34,35] These results suggest that the amidation of the N^N ligand confers significant charge-transfer character in the triplet state. Quantum chemical calculations based on time-dependent density functional theory (TD-DFT; CAM−B3LYP/LANL2DZ:6-311+G(d,p))//B3LYP/LANL2DZ:6-311+G(d,p) predict an occurrence of ligand-to-ligand charge-transfer transition, supporting this analysis (Supporting Information, Figure S2).

The phosphorescence quantum yield (Φ_p) of ZIrdap (0.016) is smaller than those of Irap (0.079) and Irp (0.10) in deaerated CH_3CN solutions, indicating that phosphorescence-quenching processes are operative in ZIrdap. As shown in Figure 2, addition of zinc ions (10 equiv in the form of $Zn(ClO_4)_2$) to the solution containing 10 μM ZIrdap produces a ca. sixfold enhancement in the phosphorescence intensity. Corresponding Φ_p value for the zinc-bound ZIrdap approaches to 0.10. Of interest is development of the distinct vibronic structures in the phosphorescence emission of the zinc-bound form of ZIrdap. This spectral signature is reminiscent of Irp (Figure 1a), suggesting that zinc binding evokes structural changes in the amide group. Actually, TD-DFT calculations show that N^N ligand-centered π−π* transition becomes dominant in the lowest triplet state upon zinc binding (Supporting Information, Figure S2). Subsequent addition of the strong zinc chelator, *N,N,N′,N′*-tetrakis(2-picolyl)ethylenediamine (TPEN), readily

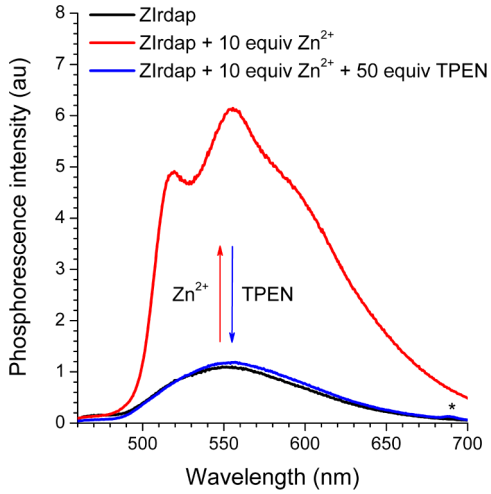

Figure 2. Phosphorescence spectra (deaerated acetonitrile solutions) of 10 μM ZIrdap in the absence (black) and presence (red) of 10 equiv of zinc ions and after the subsequent addition of 50 equiv of TPEN (blue). The asterisk (*) indicates a peak resulting from a harmonic of the excitation beam (345 nm).

restores the original spectrum, demonstrating excellent reversibility. As expected, the reference complexes without the DPA zinc receptors do not show zinc responses. Taken together, the solution behaviors suggest that modulation of PeT is most likely responsible for the phosphorescence turn-on responses to zinc ions. Photophysical data for the Ir(III) complexes are compiled in Table 1.

To estimate $-\Delta G_{PeT}$, electrochemical measurements using cyclic and differential pulse voltammetry were performed (Figure 3). The voltammograms of ZIrdap display two anodic peaks at E_{ox} = 1.05 and 1.60 V versus SCE, which correspond to oxidation of the dap ligand and the Ir(III/IV) redox process, respectively.[1,2] The former and the latter waves are also found in the dap ligand and Irap, respectively, confirming the assignments. A reversible wave at $E_{1/2}$ = −1.12 V versus SCE due to the one-electron reduction of the N^N ligand is also observed. The E^*_{red} value for the phosphorescent moiety in ZIrdap can thus be calculated to be 1.44 V versus SCE, using the ΔE_T value of 2.56 eV that was determined at the

DOI: 10.1021/acs.inorgchem.5b00967
Inorg. Chem. 2015, 54, 9704−9714

Table 1. Photophysical Data for the Phosphorescent Sensor and Its Reference Compounds

	λ_{abs} (nm; $\varepsilon \times 10^{-4}$ M^{-1} cm^{-1})[a]	λ_{ems} (nm)	Φ_p[b]	E_{ox} (V vs SCE)[c]	E_{red} (V vs SCE)[c]	E^*_{red} (V vs SCE)[d]	τ_{obs} (μs)[e]	k_r ($\times 10^4$ s^{-1})[f]	k_{nr} ($\times 10^5$ s^{-1})[g]	k_{PeT} ($\times 10^5$ s^{-1})[h]
ZIrdap	360 (1.98)	554,[a] 596[i]	0.016	1.05 (ir), 1.60 (qr)	−1.12 (r)	1.44	0.050[j]	32	200	200
+ Zn^{2+} [k]	354 (2.26)	556,[a] 572[i]	0.10	N.A.	N.A.	N.A.	6.5[j]	1.5	1.5	N.A.
Irap	357 (1.65)	555,[a] 591[i]	0.079	1.63 (r)	−1.16 (r)	1.39	1.2	6.6	6.6	N.A.
Irp	376 (1.66)	551,[a] 552[i]	0.10	1.49 (ir)	−1.40 (qr)	1.12	40	0.25	2.3	N.A.

[a] 10 μM phosphorescent compound in deaerated acetonitrile; 298 K. [b] Phosphorescence quantum yield relatively determined by employing fluorescein as the standard (0.1 N NaOH; Φ_f = 0.79). [c] Determined by cyclic voltammetry. Conditions: scan rate = 100 mV/s; 1.00 mM in Ar-saturated acetonitrile containing 100 mM Bu_4NPF_6 supporting electrolyte; a Pt wire counter and a Pt disc working electrodes; and a $Ag/AgNO_3$ couple for the pseudo reference electrode. (r) = reversible wave, (qr) = quasi reversible wave, (ir) = irreversible wave, and (N.A.) = not applicable. [d] Excited-state reduction potential, $E^*_{red} = E_{red} + \Delta E_T$. [e] Phosphorescence lifetime for 50 μM compound in deaerated acetonitrile observed at λ_{ems} = 555 nm (λ_{ex} = 377 nm). [f] Radiative rate constant (k_r) = Φ_p/τ_{obs}. [g] Nonradiative rate constant (k_{nr}) = $(1 - \Phi_p)/\tau_{obs}$. [h] Rate constant for PeT (k_{PeT}), $k_{PeT} = 1/\tau_{obs} - 1/\tau_{obs}(Zn)$, where τ_{obs} and $\tau_{obs}(Zn)$ are the observed phosphorescence lifetimes in the absence and presence of zinc ions, respectively. N.A. indicates not applicable. [i] 10 μM phosphorescent compound in air-equilibrated aqueous buffer solution (20 mM PIPES, pH = 7.4); 298 K. [j] Weighted-average phosphorescence lifetime of biexponential decays: zinc-free ZIrdap, 0.031 μs (53) and 0.79 μs (0.054); zinc-bound ZIrdap, 0.070 μs (0.58) and 7.2 μs (0.46). [k] 5 equiv of zinc ions.

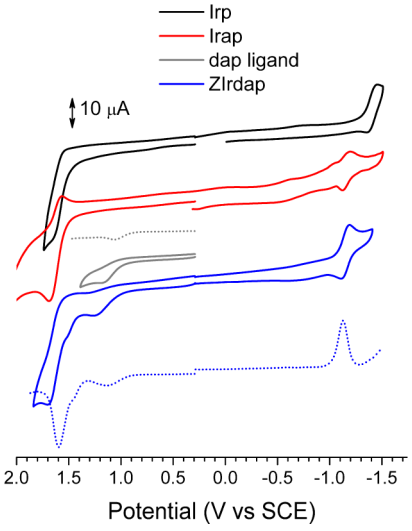

Figure 3. Cyclic (solid lines) and differential pulse (dotted lines) voltammograms of ZIrdap (blue), the dap ligand (gray), Irap (red), and Irp (black). Conditions: scan rate = 100 mV s^{-1} (cyclic voltammetry) and 4.0 mV s^{-1} (differential pulse voltammetry); 1.0 mM in Ar-saturated acetonitrile containing a 0.10 M Bu_4NPF_6 supporting electrolyte; a Pt wire counter electrode and a Pt disc working electrode; a $Ag/AgNO_3$ couple as the pseudo reference electrode.

intersection between the UV−vis absorption and phosphorescence spectra. It is noted that ZIrdap retains the E^*_{red} value similar to that (1.33−1.47 V vs SCE) of the previous blue-phosphorescent zinc probes,[1] despite the significant bathochromic shift of 2450 cm^{-1} in the phosphorescence emission. In addition, the E^*_{red} value is more positive than those of biologically useful fluorophores, including fluorescein (1.15 V vs SCE) and rhodamine B (1.25 V vs SCE),[36] providing improved margins for the occurrence of PeT from DPA. Another notable feature is the high-lying oxidation potential of the DPA moiety in ZIrdap (i.e., 1.05 V vs SCE).[1] This value is cathodically shifted from the oxidation potential of DPA in the previous zinc sensor (1.28 V vs SCE), making PeT in ZIrdap more exoergic.

The above electrochemical data reveal thermodynamic allowance ($-\Delta G_{PeT}$ = 0.39 eV) for PeT in the zinc-free form of ZIrdap. To monitor the PeT process, we acquired phosphorescence decay traces at 555 nm of 50 μM ZIrdap after nanosecond pulsed excitation at 377 nm (Figure 4). In the

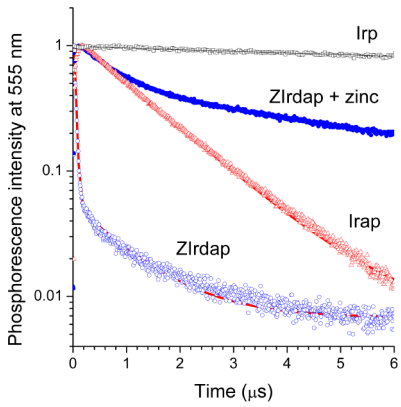

Figure 4. Photoluminescence decay traces of 50 μM Irp (□), 50 μM Irap (△), and 50 μM ZIrdap (○) in the absence (empty symbols) and presence (filled symbols) of 5 equiv of zinc ions after nanosecond pulsed photoexcitation at 377 nm. Conditions: deaerated CH_3CN solutions.

zinc-free state of ZIrdap, the transient phosphorescence signals follow a biexponential decay model with time constants of 0.031 μs (53) and 0.79 μs (0.054) (values in the parentheses are pre-exponential factors). Corresponding weighted-average lifetime (τ_{obs}) is 0.050 μs. This lifetime value is significantly shorter than those of 50 μM Irp (40 μs) and 50 μM Irap (1.2 μs). Addition of 5 equiv of zinc ions elongates the weighted-average lifetime to 6.5 μs, implying that PeT is abolished by the zinc binding. The PeT rate (k_{PeT}) is estimated to be 2.0 × 10^7 s^{-1} from the relationship $k_{PeT} = 1/\tau_{obs} - 1/\tau_{obs}(zinc)$, where τ_{obs} and $\tau_{obs}(zinc)$ are the phosphorescence lifetimes of ZIrdap in the absence and presence of zinc ions, respectively. This k_{PeT} value is comparable with the rates for electron transfer occurring between phenanthrene and dialkylamido groups in the *Z* conformation.[37] Note that the k_{PeT} value is identical to the overall nonradiative rate (k_{nr}, $k_{nr} = (1 - \Phi_p)/\tau_{obs}$ = 2.0 ×

DOI: 10.1021/acs.inorgchem.5b00967
Inorg. Chem. 2015, 54, 9704−9714

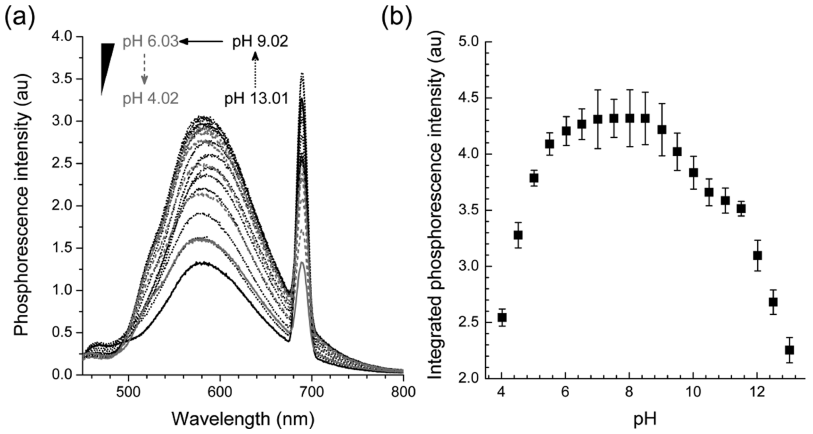

Figure 5. (a) Phosphorescence spectra of 10 μM ZIrdap in air-equilibrated water at different pH values. λ_{ex} = 345 nm. (b) A plot of the integrated (λ_{ems} = 378−800 nm) phosphorescence intensity of 10 μM ZIrdap in air-equilibrated water as a function of pH.

10^7 s^{-1}) within the experimental error. This finding supports the notion that PeT is the dominant quenching process in the zinc-free state of ZIrdap. In addition, the similarity between the k_{nr} values of Irap (6.6×10^5 s^{-1}) and the zinc-bound form of ZIrdap (1.5×10^5 s^{-1}) provides evidence for complete suppression of PeT by zinc coordination.

Zinc Detection in the Aqueous Milieu. The phosphorescence intensity in the zinc-free form of 10 μM ZIrdap in air-equilibrated aqueous buffer solutions at pH 7.4 (20 mM PIPES) is higher than the case in acetonitrile. This increased basal intensity can be ascribed to protonation of DPA. Indeed, phosphorescence titration experiments demonstrate that the integrated phosphorescence intensity starts to increase with decreasing pH (Figure 5). The phosphorescence intensity remains relatively large in the rage of pH 6−9, and decreases at pH < 6. The lower phosphorescence intensities at acidic pHs may be ascribed to decoordination of the dap ligand, because returning the pH to 7.4 does not restore the original spectrum. Actually, the electrospray ionization mass spectrometry (ESI MS; positive) spectrum of ZIrdap incubated at pH 4.0 for 1 h displays peaks corresponding to the free dap ligand and the biscyclometalated Ir complex fragment devoid of the dap ligand (i.e., $[Ir(C\text{^}N)_2]^+$; Supporting Information, Figure S3). The decoordination accompanies an appearance of a new hypsochromically shifted emission band at 380−480 nm. The spectral position and the photoluminescence lifetime of the new emission coincide with those of the dap ligand (Supporting Information, Figures S4 and S5), pointing to decoordination. These data demonstrate that ZIrdap loses its ability to detect zinc ions under prolonged exposure to acidic environments. Decoordination dynamics appears to be slow, but further investigations would be necessary to establish the kinetics of decoordination. Still, addition of 5 equiv of $ZnCl_2$ produces twofold enhancements in the phosphorescence intensities in the range of pH 5.0−8.0 (Figure 6).

The phosphorescence zinc responses could be distinguishable from the proton-induced changes, because a hypsochromic shift of 700 cm^{-1} is evoked by zinc binding (Supporting Information, Figure S6; zinc-free state, λ_{em} = 596 nm; zinc-bound state, λ_{em} = 572 nm). The zinc-induced hypsochromic shift in the phosphorescence spectrum may originate from amido-to-iminol tautomerization and binding of HO^- ion at the zinc center, as recently reported by Shiraishi and co-workers.[32] Actually, ESI MS (positive mode) spectra of the zinc-bound form of ZIrdap contained a peak at m/z = 1146.0 that

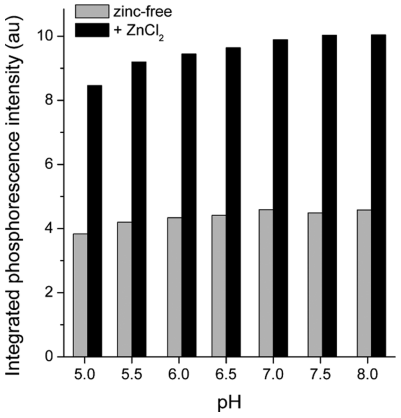

Figure 6. Phosphorescence turn-on responses of 10 μM ZIrdap to 5 equiv of zinc ions at various pH values.

corresponded to $[Zn(ZIrdap-H^+)(OH)(CH_3CN)_2]^+$ (calcd 1146.2), supporting this hypothesis (Supporting Information, Figure S7). Furthermore, TD-DFT results for this structure predicted a hypsochromic shift (645 cm^{-1}) similar to the experimental observation (Supporting Information, Figures S2). Such a hypsochromic shift upon zinc binding is not observed in acetonitrile solutions.

Phosphorescence zinc titration for 10 μM ZIrdap was performed with increasing the total zinc concentration from 0 to 15 μM at a 0.05 μM interval (Figure 7a). The phosphorescence intensity increases in proportion with the added zinc concentration and levels off after 1.0 equiv of $ZnCl_2$.

Job's plot analysis supports this 1:1 binding stoichiometry (Supporting Information, Figure S8). Corresponding zinc titration isotherm was fit to the analytical equations of the phosphorescence intensity and the free zinc concentration (eqs 1 and 2 in the Experimental Section). Iterative nonlinear least-squares fit to the equations returns the zinc dissociation constant (K_d) of 109 pM (Figure 7b). This value is 2 orders of magnitude smaller than the K_d value of the previous phosphorescence zinc sensor, indicating tight zinc binding of ZIrdap.[2] The stronger binding capability may originate from participation of the amide group in zinc coordination.[31,32]

As shown in Figure 8, the phosphorescence response of ZIrdap is selective to zinc ions over other biological metal ions. Presence of 100 mM Na, 100 mM Mg, 100 mM K, 100 mM Ca, 50 μM Cr, 50 μM Mn, and 50 μM Fe(III) ions has no

DOI: 10.1021/acs.inorgchem.5b00967
Inorg. Chem. 2015, 54, 9704−9714

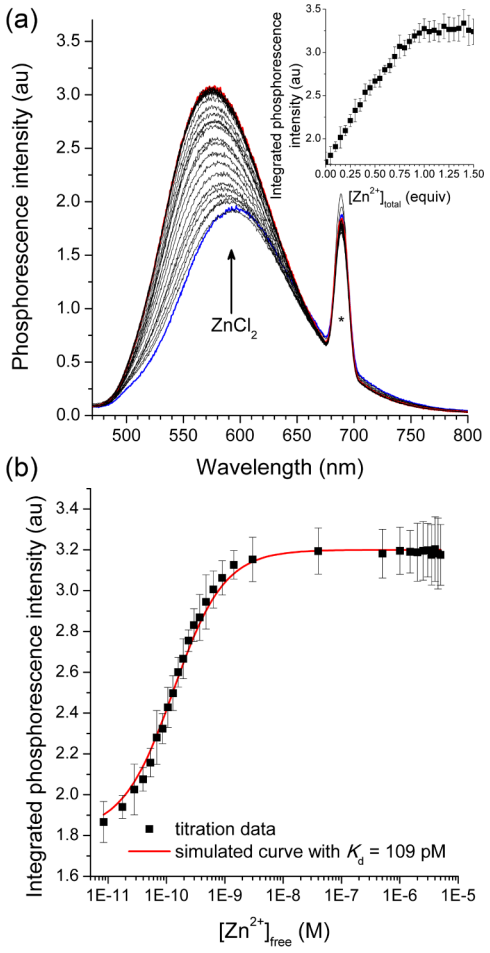

Figure 7. (a) Phosphorescence zinc response of 10 μM ZIrdap at pH 7.4 (air-equilibrated aqueous solution buffered with 20 mM PIPES). The asterisk (*) indicates a peak resulting from the second harmonic of the excitation beam (345 nm). (inset) Titration isotherm of the integrated phosphorescence intensity as a function of the total zinc concentration. (b) Titration isotherm of the integrated phosphorescence intensity as a function of the calculated concentration of free zinc. Red curve is the nonlinear least-squares fit of the titration data to eq 1 in the Experimental Section.

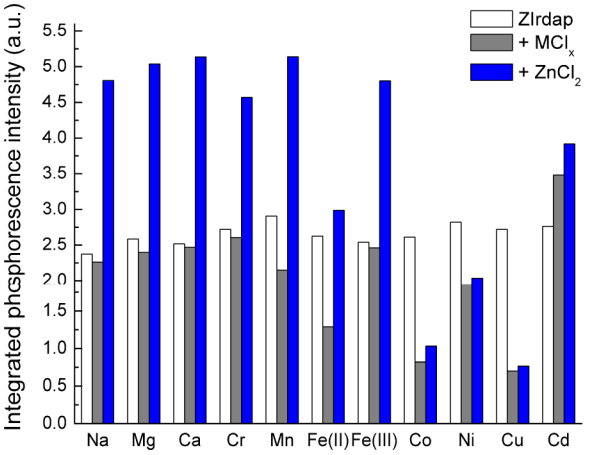

Figure 8. Phosphorescence zinc selectivity of 10 μM ZIrdap over other competing metal ions at pH 7.4 (20 mM PIPES containing 100 mM KCl): 100 mM Na, Mg, and Ca, and 50 μM Cr, Mn, Fe(II), Fe(III), Co, Ni, Cu, and Cd. 50 μM $ZnCl_2$ was added to the ZIrdap solution containing the competing metal ions.

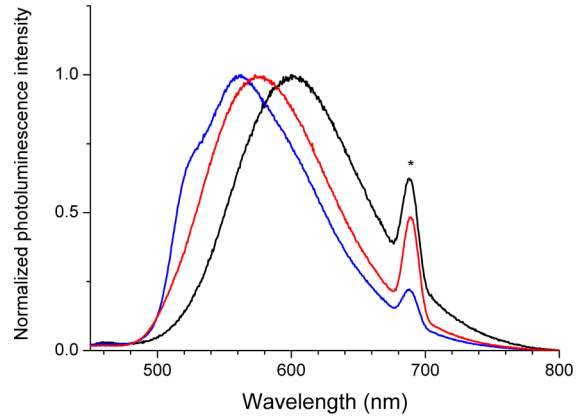

Figure 9. Phosphorescence spectra of 10 μM ZIrdap (20 mM PIPES, pH 7.4) in the absence (black) and presence (blue) of 1.5 equiv of $CdCl_2$ and 1.5 equiv of $ZnCl_2$ (red). λ_{ex} = 345 nm. The asterisk is due to the second harmonic of the excitation beam.

influence on the phosphorescence zinc (50 μM) response of 10 μM ZIrdap. Weaker responses are observed when 50 μM Fe(II) ions are present, and paramagnetic ions, including Co, Ni, and Cu, abolish the ability of ZIrdap for phosphorescence zinc detection. Similar to other zinc probes,[38−54] Cd binding produces turn-on responses. However, the interferences by these metal ions will be minimal due to low concentrations of the chelatable forms in the biological milieu.

Comparison of Zinc and Cadmium Binding Behaviors. Many zinc probes experience interferences by cadmium ions. ZIrdap also displays a phosphorescence turn-on response to Cd ions. However, as shown in Figure 9, the phosphorescence spectrum of the cadmium-bound form differs from those of zinc-free and -bound forms. The peak wavelength of the phosphorescence emission of the cadmium-bound form is 561 nm, which shifts hypsochromically from the zinc-free state by 1200 cm^{-1}. The extent of the blue shift is greater than the case for zinc binding (700 cm^{-1}). Another notable feature in the phosphorescence spectrum for the cadmium-bound form is the presence of a shoulder peak at 526 nm. This spectral signature is indicative of a Cd-binding mode different from a Zn-binding motif. Indeed, UV−vis absorption titration of ZIrdap (20 mM PIPES, pH 7.4) with increasing either $ZnCl_2$ or $CdCl_2$ concentrations revealed different spectral profiles. As shown in Figure 10, the metal-free ZIrdap exhibits the lowest-energy absorption band at 346 nm. The additions of $CdCl_2$ and $ZdCl_2$ lead to bathochromic shifts of the absorption band with multiple isosbestic points ($CdCl_2$, 358, 318, and 303 nm; $ZnCl_2$, 365, 301, and 273 nm). These red shifts are opposite to the blue shifts in the phosphorescence spectra (Figure 9), suggesting that polar ground states are formed upon metal binding. In the case of the cadmium titration, the absorbance at 337 nm decreases in a monotonic manner and reached a plateau after 1 equiv of Cd ions (Figure 10a,c). Similar linear behaviors are observed in the phosphorescence cadmium titration experiments (Figure 11). In sharp contrast, zinc titration produces two-stage spectral changes (Figure 10b,c). The incremental addition of $ZnCl_2$ up to 0.5 equiv yields absorption changes identical to the spectral signatures of the cadmium titration. Further addition of $ZnCl_2$ evokes the second absorption responses with a hypsochromic shift in the peak wavelength. An isosbestic point at 349 nm is observed, indicating that the second response is not due to instrumental

DOI: 10.1021/acs.inorgchem.5b00967
Inorg. Chem. 2015, 54, 9704−9714

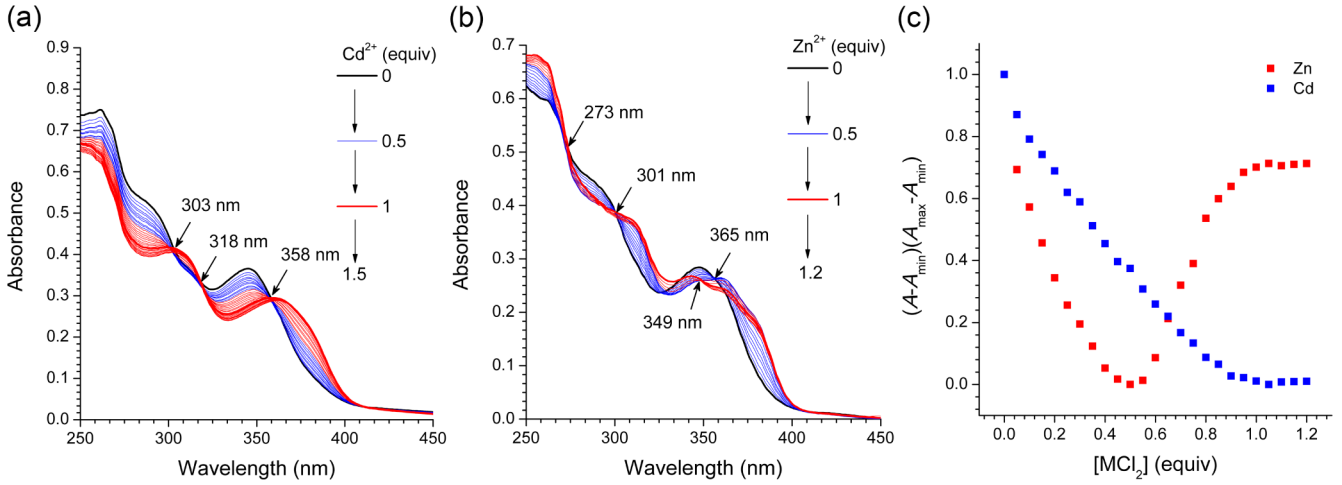

Figure 10. UV−vis absorption titration of 10 μM ZIrdap with $CdCl_2$ (a) and $ZnCl_2$ (b) in 20 mM PIPES buffer at pH 7.4, and corresponding titration isotherms for cadmium and zinc monitored at 337 nm (c).

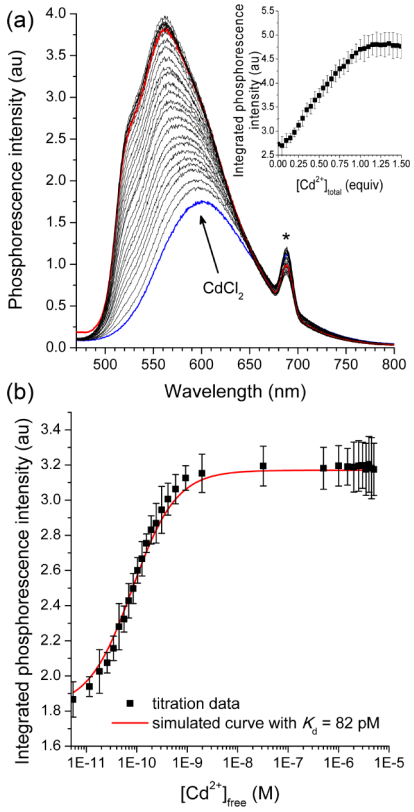

Figure 11. (a) Phosphorescence cadmium response of 10 μM ZIrdap at pH 7.4 (air-equilibrated aqueous solution buffered with 20 mM PIPES). The asterisk (*) indicates a peak resulting from the second harmonic of the excitation beam (345 nm). (inset) Titration isotherm of the integrated phosphorescence intensity as a function of the total cadmium concentration. (b) Titration isotherm of the integrated phosphorescence intensity as a function of the calculated concentration of free cadmium. Red curve is the nonlinear least-squares fit of the titration data to eq 1 in the Experimental Section.

drifts. The titration isotherm plotting the absorbance at 337 nm versus the added $ZnCl_2$ concentration reveals the zinc response that is different from the cadmium case (Figure 10c).

To obtain insight into the binding geometries, ^{1}H NMR spectra were obtained for ZIrdap in the absence and presence of zinc and cadmium ions (Supporting Information, Figure 9). Although the complexity of the NMR spectra hampers complete assignments, the NMR spectra may suggest that the Cd-bound form retains the amido tautomer of the metal-free ZIrdap, whereas zinc binding induces the amido-to-iminolate tautomerization. Several attempts to obtain crystals for the metal-bound forms were not successful. On the basis of the results, it is proposed that ZIrdap adopts a predominant 2:1 (ZIrdap/Zn) binding geometry at low zinc concentrations (i.e., <0.5 equiv), where the amido form of ZIrdap is involved. At high zinc concentrations, a 1:1 complex having the iminolate form becomes the dominant species. This hypothesis is supported by the ESI MS and TD-DFT results for the zinc-bound ZIrdap (Supporting Information, Figures S2 and S7). However, further investigations should be performed to fully elucidate the structure−photophysical response relationship, because the phosphorescence zinc titration exhibits the one-stage (i.e., monotonic) increase in the phosphorescence intensity (Figure 7).

Finally, the cadmium dissociation constant (K_d) was determined using the phosphorescence titration results. Nonlinear least-squares fit of the titration data to eqs 1 and 2 in the Experimental Section yields a K_d value of 82 pM. This value is comparable to the K_d for zinc binding, implying that ZIrdap binds cadmium ions as strong as zinc ions.

Visualization of Intracellular Zinc. Having established the ability of ZIrdap for phosphorescence zinc detection, we sought to demonstrate bioimaging utility of the zinc probe (Figure 12). HeLa, human cervical cancer cells, were employed for the intracellular zinc imaging experiments. ZIrdap is permeable through the membrane of HeLa cells, as evidenced by phosphorescence halos (λ_{ex} = 405 nm and λ_{ems} = 441−691 nm) in the cytosol of HeLa cells pretreated with 10 μM ZIrdap (10 min). The spectral profile of the intracellular phosphorescence signals resembles the phosphorescence spectrum of the zinc-bound form of ZIrdap recorded in acetonitrile (Figure 12c), confirming that the ZIrdap is responsible for the photoemission.[55] The non-negligible phosphorescence intensity might be due to protonation or endogenous zinc levels in HeLa cells comparable to the K_d value of ZIrdap.[56] Addition of the ionomeric form of zinc ions (50 μM $ZnCl_2$ + 100 μM sodium pyrithione) leads to a prompt increase in the phosphorescence intensity (Figure 12a). The corresponding

DOI: 10.1021/acs.inorgchem.5b00967
Inorg. Chem. 2015, 54, 9704−9714

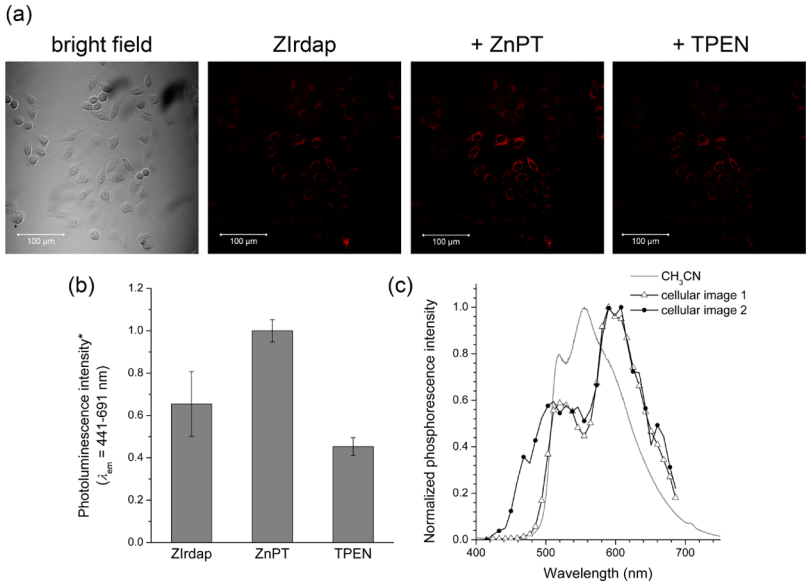

Figure 12. Phosphorescence visualization of exogenously supplied zinc ions in the form of ZnPT ($ZnCl_2$/sodium pyrithione = 1:2, mol/mol). (a) From the left: bright field image, HeLa cells incubated with 10 μM ZIrdap for 10 min, cells subsequently treated with 50 μM ZnPT, after the successive treatment with 100 μM TPEN. λ_{em} = 441−691 nm (λ_{ex} = 405 nm). Scale bar = 100 μm. (b) Average photoluminescence intensities of the HeLa cells treated with 10 μM ZIrdap (left) and after subsequent treatment with 50 μM ZnPT (middle), followed by 100 μM TPEN addition (right). The photoluminescence intensities of the ZnPT-treated cell images were normalized to 1. Averages of 11 experiments. (c) Comparison of the phosphorescence spectrum (gray line) of the zinc-bound ZIrdap (CH_3CN) and the λ-profiles of the photoluminescence emission from the ZIrdap-treated HeLa cells before (●) and after (△) the ZnPT addition. More photoluminescence cell images are included in the Supporting Information, Figure S10.

phosphorescence turn-on ratio as quantitated by an average of 11 dishes is 1.5 (Figure 12b), barely enabling zinc imaging. Validity of the phosphorescence turn-on responses was assessed by the fluorescence-activated cell sorting (FACS) analyses (Supporting Information, Figure S11). Subsequent addition of 100 μM TPEN reduces the phosphorescence intensities, confirming zinc responses.

One drawback of using ZIrdap in live cell imaging is noted: ZIrdap is cytotoxic to HeLa cells upon prolonged exposure (>30 min) to the photoexcitation beam. We speculated that this phototoxicity might result from photosensitization of singlet dioxygen ($^1O_2$) by ZIrdap.[57] Indeed, the quantum yields for singlet oxygen photogeneration (Φ_Δ) of both zinc-free and zinc-bound forms of ZIrdap, determined using methylene blue (Φ_Δ = 0.52)[58] and 1,3-diphenylisobenzofuran[59] as the standard and the $^1O_2$-selective substrate, respectively, approach unity (Supporting Information, Figure S12). The Φ_Δ values for Irap and Irp are also as high as 0.89 and 0.68, respectively, indicating that the cyclometalated Ir(III) complexes are responsible for the $^1O_2$ photosensitization. These results present an additional challenge to the establishment of molecular strategies to attenuate phototoxicity of phosphorescent probes.

III. SUMMARY AND CONCLUSIONS

It has remained as a significant challenge to develop red-phosphorescent probes that can reversibly detect biological zinc ions. This difficulty stems from the thermodynamic forbiddance of PeT in the probes with low-energy phosphorescence emission. We have developed a zinc probe (ZIrdap) that is capable of producing fully reversible turn-on responses in the low-energy phosphorescence regions. The molecular construct for the phosphorescent probe involved the biscyclometalated Ir(III) complex and the DPA-appended 2-(2-pyridyl)pyrazine N^N ligand. An amide linkage was employed for bridging DPA and 2-(2-pyridyl)pyrazine. This ligand structure had two effects on the thermodynamic parameters of PeT: One was increasing E^*_{red} of the phosphorescent center, and the other was decreasing E_{ox} of DPA. The net result of these two effects was exothermicity of PeT ($-\Delta G_{PeT}$ = 0.39 eV) at a significantly small phosphorescence energy (λ_{ems} = 596 nm). We monitored the occurrence of the intramolecular PeT and determined the PeT rate to be 2.0×10^7 s^{-1}, by employing transient photoluminescence techniques. This PeT rate was virtually identical to the overall rate of nonradiative transition in the zinc-free form of ZIrdap, indicating the effectiveness of PeT in the phosphorescence modulation. The zinc probe produced turn-on responses, which were fully reversible and selective to zinc ions over other biological metal ions. However, similar turn-on phosphorescence signaling was evoked by cadmium ion, while titration experiment results suggested different metal-binding modes. Finally, the probe was capable of visualizing exogenously supplied zinc ions in live HeLa cells. Despite the advance, however, one challenge to attenuation of $^1O_2$-mediated phototoxicity remains. This calls for future studies to establish molecular strategies for the minimization of $^1O_2$ sensitization.

IV. EXPERIMENTAL SECTION

Materials and Synthesis. ***Caution!*** *Perchlorate salts of metal complexes are potentially explosive. Only small quantities of material should be handled with care.* The chloride-bridged Ir(III) precursor $[(dfppy)_2Ir(\mu\text{-}Cl)]_2$ (dfppy = 2-(2,4-difluorophenyl)pyridinate) was synthesized according to a literature method.[60] Commercially available chemicals were used as received. All glassware and magnetic stirring bars were thoroughly dried in a convection oven. Reactions were monitored using thin layer chromatography (TLC). Commercial TLC plates (silica gel 254, Merck Co.) were developed, and the spots were visualized under UV light at 254 or 365 nm. Silica gel column chromatography was performed with silica gel 60 G (particle size

DOI: 10.1021/acs.inorgchem.5b00967
Inorg. Chem. 2015, 54, 9704−9714

0.063−0.200 mm, Merck Co.). ^{1}H, ^{13}C, and ^{19}F NMR spectra were collected with Bruker Ultrashield 300 and 400 Plus NMR spectrometers and referenced to residual proton peaks of the deuterated solvent. Mass spectra were recorded using a Thermo Electrons Co. Finnigan LCQ Advantage Max spectrometer and a JEOL JMS-600W mass spectrometer. Elemental analysis was performed using CE Instrument EA1110 and EA1112 for C, H, and N.

2-Amino-5-(2-pyridyl)pyrazine. 2-Amino-5-bromopyrazine (2.60 g, 17.0 mmol), 2-(tributylstannyl)pyridine (6.19 g, 19.0 mmol), and tetrakis(triphenylphosphine)palladium(0) (1.76 g, 1.70 mmol) were dissolved in toluene (120 mL), and the solution was refluxed for 1 d under an Ar atmosphere. After it cooled to room temperature, the reaction mixture was concentrated and subjected to chromatographic purification on silica gel column (CH_2Cl_2/CH_3OH = 49:1 to 9:1, v/v). Yellowish-brown powder (2.30 g, 78%). ^{1}H NMR ($CDCl_3$, 400 MHz) δ: 4.71 (s, 2H), 7.23−7.25 (m, 1H), 7.79 (t, J = 7.7 Hz, 1H), 8.03 (d, J = 1.4 Hz, 1H), 8.16 (d, J = 8.0 Hz, 1H), 8.64 (d, J = 4.8 Hz, 1H), 9.06 (d, J = 1.4 Hz, 1H). ^{13}C NMR ($CDCl_3$, 100 MHz) δ: 119.73, 122.79, 130.83, 136.83, 140.81, 141.71, 149.17, 154.16, 154.98. HR MS (EI, positive): Calcd for $C_9H_8N_4$, 172.0749; found: 172.0746. Anal. Calcd for $C_9H_8N_4$: C, 62.78; H, 4.68; N, 32.54. Found: C, 62.71; H, 4.72; N, 32.21%.

2-(Bromoacetylamino)-5-(2-pyridyl)pyrazine. 2-Amino-5-(2-pyridyl)pyrazine (0.500 g, 2.90 mmol) and K_2CO_3 (0.480 g, 3.50 mmol) were dissolved in an anhydrous acetonitrile (50 mL). Bromoacetyl bromide (276 μL, 3.20 mmol) was added to a stirred solution of the reaction mixture, which was stirred additionally for 16 h at room temperature. After removal of the solvent, the concentrated mixture was subjected to silica gel column chromatography (CH_2Cl_2 to CH_2Cl_2/CH_3OH = 9:1, v/v) to give a yellow powder (0.460 g, 54%). ^{1}H NMR ($CDCl_3$, 400 MHz) δ: 4.08 (s, 2H), 7.33−7.36 (m, 1H), 7.86 (t, J = 7.6 Hz, 1H), 8.36 (d, J = 8.0 Hz, 1H), 8.70 (d, J = 4.8 Hz, 1H), 9.36 (d, J = 1.2 Hz, 1H), 9.53 (d, J = 1.2 Hz, 1H). ^{13}C NMR (deuterated dimethyl sulfoxide (DMSO), 100 MHz) δ: 31.12, 61.94, 122.22, 125.80, 135.43, 141.58, 148.05, 149.58, 150.95, 165.46, 172.57. HR MS (EI, positive): Calcd for $C_{11}H_9N_4OBr$, 291.9960; found: 291.9957. Anal. Calcd for $C_{11}H_9N_4OBr$: C, 45.07; H, 3.09; N, 19.11. Found: C, 44.82; H, 3.06; N, 19.29%.

2-((Di(2-picolyl)amino)acetylamino)-5-(2-pyridyl)pyrazine. An acetonitrile solution (50 mL) containing 2-(bromoacetylamino)-5-(2-pyridyl)pyrazine (0.194 g, 0.662 mmol), di(2-picolyl)amine (0.120 g, 0.602 mmol), and K_2CO_3 (0.128 g, 0.927 mmol) was stirred for 1 d at room temperature. The reaction mixture was filtered to remove residual K_2CO_3, and the filtrate was concentrated. Chromatographic purification on silica gel column (CH_2Cl_2 to CH_2Cl_2/CH_3OH = 9:1, v/v) gave a brown powder (0.220 g, 88%). ^{1}H NMR ($CDCl_3$, 400 MHz) δ: 3.59 (s, 2H), 4.04 (s, 4H), 7.17−7.20 (m, 2H), 7.30−7.32 (m, 1H), 7.36 (d, J = 8.0 Hz, 2H), 7.66 (t, J = 7.6 Hz, 2H), 7.84 (t, J = 7.6 Hz, 1H), 8.33 (d, J = 8.0 Hz, 1H), 8.67 (d, J = 4.8 Hz, 2H), 8.70 (d, J = 4.8 Hz, 1H), 9.40 (d, J = 1.6 Hz, 1H), 9.54 (d, J = 1.2 Hz, 1H). ^{13}C NMR ($CDCl_3$, 100 MHz) δ: 59.06, 60.80, 120.92, 122.56, 123.15, 123.71, 135.32, 136.77, 137.05, 140.88, 146.42, 148.34, 149.29, 149.48, 154.47, 157.94, 171.18, 207.01. HR MS (FAB, positive, m-NBA): Calcd for $C_{23}H_{21}ON_7$, 411.1808; found: 411.1818.

ZIrdap. An anhydrous CH_2Cl_2 (40 mL) solution containing the chloride-bridged Ir(III) dimer ($[(dfppy)_2Ir(\mu\text{-}Cl)]_2$; 0.350 g, 0.290 mmol) and 2-((di(2-picolyl)amino)acetylamino)-5-(2-pyridyl)-pyrazine (0.200 g, 0.490 mmol) was refluxed for 6 h under an Ar atmosphere. The reaction mixture was cooled to room temperature, and NH_4PF_6 (15 equiv) was slowly added to the solution. After 12 h, the reaction mixture was filtered to remove NH_4PF_6 and concentrated under vacuum. The crude mixture was subjected to flash column chromatography on silica gel with CH_2Cl_2 to CH_2Cl_2/CH_3OH = 19:1 (v/v). Further purification by preparative TLC techniques was performed to isolate an orange powder (0.290 g, 44%). ^{1}H NMR (CD_3CN, 300 MHz) δ: 3.50 (d, J = 3.6 Hz, 2H), 3.97 (s, 4H), 5.71 (m, 2H), 6.68−6.76 (m, 2H), 7.07−7.20 (m, 4H), 7.26 (d, J = 7.8 Hz, 2H), 7.51 (m, 1H), 7.62 (m, 3H), 7.73 (m, 1H), 7.90−7.99 (m, 3H), 8.17 (td, J = 7.8, 1.5 Hz, 1H), 8.32 (d, J = 8.7 Hz, 2H), 8.52 (d, J = 8.1 Hz, 1H), 8.57 (m, 2H), 8.85 (d, J = 1.2 Hz, 1H), 9.50 (d, J = 1.2 Hz, 1H). ^{13}C NMR ($CDCl_3$, 100 MHz) δ: 59.56, 60.50, 114.04, 122.73, 122.80, 123.83, 124.01, 124.77, 127.70, 134.98, 136.96, 139.32, 140.43, 144.50, 145.85, 148.84, 149.03, 149.51, 149.82, 151.99, 152.76, 154.22, 157.72, 172.69, 206.97. ^{19}F NMR ($CDCl_3$, 376 MHz) δ: −108.25 (m, 2F), −105.02 (m, 2F), −73.00 (d, J = 771 Hz, 6F). HR MS (FAB, positive, m-NBA): Calcd for $C_{45}H_{33}F_4IrN_9O$ ($[M-PF_6]^+$), 984.2373; found: 984.2370.

Irp. The identical method for the synthesis of ZIrdap was employed, except using 2-amino-5-(2-pyridyl)pyrazine instead of 2-((di(2-picolyl)amino)acetylamino)-5-(2-pyridyl)pyrazine. 0.210 g (29%). ^{1}H NMR (CD_2Cl_2, 400 MHz) δ: 5.65 (s, 2H), 5.74 (t, J = 9.7 Hz, 2H), 6.64 (t, J = 9.2 Hz, 2H), 7.09 (t, J = 7.2 Hz, 1H), 7.15 (t, J = 7.3 Hz, 1H), 7.29 (s, 1H), 7.39 (t, J = 6.8 Hz, 1H), 7.48 (d, J = 5.8 Hz, 1H), 7.70 (d, J = 5.7 Hz, 1H), 7.85−7.89 (m, 3H), 8.08 (t, J = 8.0 Hz, 1H), 8.28 (d, J = 8.3 Hz, 1H), 8.31−8.37 (m, 2H), 9.10 (s, 1H). ^{13}C NMR (CD_2Cl_2, 100 MHz) δ: 99.38, 99.65, 99.94, 100.21, 114.18, 114.36, 114.49, 114.66, 122.21, 124.13, 124.21, 124.30, 124.42, 124.63, 126.93, 127.93, 128.12, 132.15, 138.92, 139.78, 139.87, 140.10, 145.90, 148.99, 149.20, 150.52, 152.72, 153.51, 155.28, 158.20, 160.72, 164.31, 164.83, 165.47. ^{19}F NMR (CD_2Cl_2, 376 MHz) δ: −108.69 (m, 2F), −106.13 (m, 2F), −73.03 (d, J = 768 Hz, 6F). HR MS (FAB, positive, m-NBA): Calcd for $C_{31}H_{20}F_4IrN_6$ ($[M-PF_6]^+$), 745.1315; found: 745.1312.

2-(Acetylamino)-5-(2-pyridyl)pyrazine. An anhydrous acetonitrile solution (30 mL) containing 2-amino-5-(2-pyridyl)pyrazine (0.150 g, 0.870 mmol) and K_2CO_3 (0.220 g, 0.159 mmol) was stirred at room temperature for 30 min. Acetyl bromide (97.0 μL, 1.30 mmol) was added to the solution, which was stirred for additional 4 h. The reaction mixture was concentrated under reduced pressure and subjected to column purification on silica gel (CH_2Cl_2 to CH_2Cl_2/CH_3OH = 19:1, v/v). Yellowish-white powder (0.0690 g, 37%). ^{1}H NMR ($CDCl_3$, 400 MHz) δ: 2.28 (s, 3H), 7.31−7.34 (m, 1H), 7.85 (t, J = 7.6 Hz, 1H), 7.91 (s, 1H), 8.34 (d, J = 8.0 Hz, 1H), 8.69 (d, J = 4.8 Hz, 1H), 9.29 (d, J = 1.2 Hz, 1H), 9.55 (s, 1H). ^{13}C NMR ($CDCl_3$, 100 MHz) δ: 24.50, 120.99, 121.86, 123.92, 135.12, 137.11, 140.45, 146.98, 147.51, 149.28, 149.63, 168.40. HR MS (CI, positive): Calcd for $C_{11}H_{11}N_4O$ ($[M + H]^+$), 215.0933; found: 215.0938. Anal. Calcd for $C_{11}H_{10}N_4O$: C, 61.67; H, 4.71; N, 26.15. Found: C, 61.43; H, 4.68; N, 25.97%.

Irap. The identical method for the synthesis of ZIrdap was employed, except using 2-(acetylamino)-5-(2-pyridyl)pyrazine instead of 2-((di(2-picolyl)amino)acetylamino)-5-(2-pyridyl)pyrazine. 0.560 g (37%). ^{1}H NMR (CD_2Cl_2, 400 MHz) δ: 2.11 (s, 3H), 5.64−5.70 (m, 2H), 6.52−6.62 (m, 2H), 6.97−7.04 (m, 2H), 7.39 (d, J = 5.8 Hz, 1H), 7.42−7.46 (m, 1H), 7.49 (d, J = 5.8 Hz, 1H), 7.80 (t, J = 7.2 Hz, 2H), 7.92 (d, J = 5.2 Hz, 1H), 8.11 (t, J = 7.6 Hz, 1H), 8.27 (d, J = 8.4 Hz, 2H), 8.36 (s, 1H), 8.43 (d, J = 8.0 Hz, 1H), 8.84 (d, J = 1.2 Hz, 1H), 9.33 (d, J = 1.2 Hz, 1H). ^{13}C NMR (CD_2Cl_2, 100 MHz) δ: 24.74, 99.93, 114.61, 124.42, 124.54, 128.76, 135.87, 140.02, 140.11, 140.72, 145.35, 145.49, 149.25, 149.42, 151.18, 152.55, 154.32, 169.67. ^{19}F NMR (CD_2Cl_2, 376 MHz) δ: −108.74 (m, 2F), −106.08 (m, 2F), −73.02 (d, J = 770 Hz, 6F). HR MS (FAB, positive, m-NBA): Calcd for $C_{33}H_{22}F_4IrN_6O$ ($[M-PF_6]^+$), 787.1420; found: 787.1421. Anal. Calcd for $C_{33}H_{22}F_{10}IrN_6OP$: C, 42.54; H, 2.38; N, 9.02. Found: C, 42.82; H, 2.45; N, 9.04%.

Spectroscopic Measurements. Milli-Q grade water (18.2 MΩ·cm) was used to prepare solutions for spectroscopic measurements. PIPES (≥ 99%) was purchased from Aldrich. A pH 7.4 buffer solution was prepared by dissolving PIPES (20 mM) in milli-Q water and adjusting the pH with standard KOH solution (45 wt %, Aldrich) or concentrated HCl (Aldrich). The buffer solution was further treated with Chelex 100 resin (BIO-RAD) to remove trace metal ions, filtered through a membrane (pore size = 0.45 μm), and its pH was reexamined prior to use. Fresh metal stock solutions (typically, 0.10 or 0.010 M except for $CrCl_3{\cdot}6H_2O$) were prepared in milli-Q water using the corresponding chloride salts: $CuCl_2$ (99.999%, Aldrich), NaCl (≥99.5%, Aldrich), KCl (puratonic grade, Calbiochem), $MgCl_2$ (99.99%, Aldrich), $CaCl_2$ (99.99%, Aldrich), $CrCl_3{\cdot}6H_2O$ (98%, Aldrich), $MnCl_2$ (99.99%, Aldrich), $FeCl_2$ (99.99%, Aldrich), $CoCl_2$ (99.9%, Aldrich), $NiCl_2$ (99.99%, Aldrich), $CdCl_2$ (99.99%, Aldrich),

DOI: 10.1021/acs.inorgchem.5b00967
Inorg. Chem. 2015, 54, 9704−9714

and $ZnCl_2$ (99.999%, Aldrich). A TPEN solution was prepared by dissolving *N*,*N*,*N*′,*N*′-tetrakis(2-picolyl)ethylenediamine (≥99%, Sigma) in DMSO (99.9%, Aldrich). $Zn(ClO_4)_2{\cdot}6H_2O$ (Aldrich) was dissolved in CH_3CN (spectrophotometric grade, Aldrich) to 1.0, 10, and 100 mM concentrations. The Ir(III) complex solutions were prepared by dissolution in CH_3CN to concentrations of 10 mM, 1.0 mM, 100 μM, and 10 μM. The 10 μM solutions were used for spectroscopic measurements, otherwise stated. For aqueous solutions, 3.0 mL of the PIPES buffer and 3 μL of the Ir(III) complex solution (10 mM in DMSO) were mixed to give a 10 μM solution. A 1 cm × 1 cm fluorimeter cell (Hellma) with a rubber cap was used for the steady-state optical measurements. UV−vis absorption spectra were collected on a Varian Cary 50 spectrophotometer at room temperature. Phosphorescence spectra were obtained using a Quanta Master 40 scanning spectrofluorimeter at room temperature. The photoluminescence quantum yields (Φ) were relatively determined according to following standard equation: $\Phi = \Phi_{ref} \times (I/I_{ref}) \times (A_{ref}/A) \times (n/n_{ref})^2$, where *A*, *I*, and *n* are the absorbance at the excitation wavelength, integrated photoluminescence intensity, and the refractive index of the solvent, respectively. Fluorescein as an aqueous 0.1 N NaOH solution was used as the external reference ($\Phi_{ref} = 0.79$). The refractive index of the 0.1 N NaOH solution was assumed to be identical to the value for pure water. The 10 μM solutions were deaerated by bubbling Ar prior to performing the measurements. Ar-saturated 50 μM solutions (CH_3CN) were used for the determination of the phosphorescence lifetimes (τ_{obs}). Photoluminescence decay traces were acquired based on time-correlated single photon counting techniques using a FluoTime 200 instrument (PicoQuant, Germany). A 377 nm diode laser (PicoQuant, Germany; pulse energy = 35 pJ) with a repetition rate of 125 kHz was used as the excitation source. The signals at 555 nm were obtained using an automated motorized monochromator, and recorded with a NanoHarp unit. The decay profiles were analyzed (OriginPro 8.0, OriginLab) using a single or double exponential decay model.

Electrochemical Measurements. Cyclic and differential pulse voltammetry experiments were performed using a CHI630 B instrument (CH Instruments, Inc.) using three-electrode cell assemblies. A Pt wire and a Pt disc were used as the counter and working electrodes, respectively. A $Ag/AgNO_3$ couple was used as a pseudo reference electrode. Measurements were performed in Ar-saturated CH_3CN (3 mL) using tetra-*n*-butylammonium hexafluorophosphate (Bu_4NPF_6) as the supporting electrolyte (0.10 M) at scan rates of 100 mV s^{-1} (cyclic voltammetry) and 4 mV s^{-1} (differential pulse voltammetry). The concentration of the Ir(III) complex was 1.0 mM. A ferrocenium/ferrocene reference was employed as the external reference.

Determination of K_d. An approach previously reported by us[2,61] was used to determine K_d values for Zn(II) and Cd(II) binding to ZIrdap. An equilibrium model for formation of a 1:1 ligand/metal complex was applied. Mass balance equations for the total concentrations of sensor and metal ions (M^{2+}; M = Zn or Cd) can be expressed by eqs 1 and 2.

$$\text{phosphorescence intensity(P. I.)} = [\text{ZIrdap}]_{total} \times (\alpha_1 K_d + \alpha_2[M^{2+}]_{free})/(K_d + [M^{2+}]_{free}) \quad (1)$$

$$[M^{2+}]_{free}^{\ 2} + ([\text{ZIrdap}]_{total} + K_d - [M^{2+}]_{total})[M^{2+}]_{free} - K_d[M^{2+}]_{total} = 0 \quad (2)$$

In eq 1, α_1 = P.I./$[\text{ZIrdap}]_{total}$ = 1.82 × 10^{11} M^{-1} (without metal ions ions) and α_2 = P.I./$[\text{ZIrdap}]_{total}$ = 3.20 × 10^{11} M^{-1} (in the presence of an excess amount of zinc ions) and 3.17 × 10^{11} M^{-1} (in the presence of an excess amount of cadmium ions) were employed. A nonlinear least-squares method was applied to fit the metal ion titration data to eq 1 for the determination of K_d, which subsequently gave a set of free metal ion concentrations ($[M^{2+}]_{free}$) by applying eq 2. The free metal ion concentration was used to revise the K_d. This process was iterated (i.e., K_d and $[Mn^{2+}]_{free}$) until the r^2 value of the nonlinear least-squares fit could not be improved. A nonlinear curve fitting module embedded in OriginPro 8.5 (OriginLab) was used for this purpose.

Cell Culture. HeLa cells were cultured in DMEM supplemented with 10% fetal bovine serum and penicillin (100 units/mL) at 37 °C in a humidified incubator under 5% CO_2. One day before imaging, cells were passed and plated onto poly(D-lysine)-coated glass-bottom culture dishes.

Confocal Laser Scanning Microscopy. After the cells were washed with fresh DMEM, a 10 μM ZIrdap in DMSO (biotech grade, Aldrich) was added to the culture media. The cells were incubated for 10 min at 37 °C. The incubated cells were washed twice with fresh DMEM (serum-free), and photoluminescence micrographs were taken using a Carl Zeiss LSM 510 META confocal laser scanning microscope using a Newport MaiTai eHP DeepSee multiphoton excitation system. An excitation beam (405 nm) was focused onto the dish, and the signals were acquired through 30 emission channels covering the range of 441−691 nm. The cells were imaged after subsequent treatment with 50 μM $ZnCl_2$/NaPT. Finally, 100 μM TPEN (DMSO) was introduced. ZnPT and TPEN were added directly into the culture media. Exposure to the excitation beam was kept as short as possible (<10 min) to minimize photoinduced cell death. Photoluminescence images and mean intensities were processed using the ZEN and ImageJ software, respectively.

■ ASSOCIATED CONTENT

Ⓢ Supporting Information

The Supporting Information is available free of charge on the ACS Publications website at DOI: 10.1021/acs.inorgchem.5b00967.

^1H, ^{13}C, and ^{19}F NMR spectra, UV−vis absorption spectra, a summary of TD-DFT calculation results, pH titration results, FACS analysis data, phosphorescence zinc responses at different pH values, ESI MS spectrum of the zinc-bound from of ZIrdap, ^1H NMR titration with varying the zinc concentration, additional ^1H NMR spectra of ZIrdap in different solvents, phosphorescence Job's plot, phosphorescence responses to cadmium ions, more cell images, Cartesian coordinates of optimized geometries, and determination of the quantum yields for $^1O_2$ photosensitization. (PDF)

■ AUTHOR INFORMATION

Corresponding Authors

*E-mail: odds2@ewha.ac.kr. (Y.Y.)
*E-mail: wwnam@ewha.ac.kr. (W.N.)

Notes

The authors declare no competing financial interest.

■ ACKNOWLEDGMENTS

Authors acknowledge the financial support from CRI (NRF-2012R1A3A2048842 to W.N.), GRL (NRF-2010-00353 to W.N.), GFP (CISS-2012M3A6A6054204 to Y.Y.), and the Ewha Womans Univ. (1-2015-0447-001-1 to Y.Y.).

■ REFERENCES

(1) Woo, H.; Cho, S.; Han, Y.; Chae, W.-S.; Ahn, D.-R.; You, Y.; Nam, W. *J. Am. Chem. Soc.* **2013**, *135*, 4771−4787.
(2) You, Y.; Lee, S.; Kim, T.; Ohkubo, K.; Chae, W.-S.; Fukuzumi, S.; Jhon, G.-J.; Nam, W.; Lippard, S. J. *J. Am. Chem. Soc.* **2011**, *133*, 18328−18342.
(3) Ru, J.; Chen, X.; Guan, L.; Tang, X.; Wang, C.; Meng, Y.; Zhang, G.; Liu, W. *Anal. Chem.* **2015**, *87*, 3255−3262.
(4) Ulbricht, C.; Beyer, B.; Friebe, C.; Winter, A.; Schubert, U. S. *Adv. Mater.* **2009**, *21*, 4418−4441.
(5) You, Y.; Nam, W. *Chem. Soc. Rev.* **2012**, *41*, 7061−7084.

DOI: 10.1021/acs.inorgchem.5b00967
Inorg. Chem. 2015, 54, 9704−9714

(6) Zhao, Q.; Li, F.; Huang, C. *Chem. Soc. Rev.* **2010**, *39*, 3007−3030.
(7) Baggaley, E.; Weinstein, J. A.; Williams, J. A. G. *Coord. Chem. Rev.* **2012**, *256*, 1762−1785.
(8) Ruggi, A.; Reinhoudt, D. N.; Velders, A. H. *Bioinorg. Med. Chem.* **2011**, 383−406.
(9) Fernandez-Moreira, V.; Thorp-Greenwood, F. L.; Coogan, M. P. *Chem. Commun.* **2010**, *46*, 186−202.
(10) Chi, Y.; Chou, P.-T. *Chem. Soc. Rev.* **2010**, *39*, 638−655.
(11) Zhao, Q.; Huang, C.; Li, F. *Chem. Soc. Rev.* **2011**, *40*, 2508−2524.
(12) Lo, K. K.-W.; Louie, M.-W.; Zhang, K. Y. *Coord. Chem. Rev.* **2010**, *254*, 2603−2622.
(13) Lo, K. K.-W. *Topics in Organometallic Chemistry* **2010**, *29*, 115−158.
(14) Lo, K. K.-W.; Zhang, K. Y. *RSC Adv.* **2012**, *2*, 12069−12083.
(15) Lo, K. K.-W.; Zhang, K. Y.; Li, S. P.-Y. *Pure Appl. Chem.* **2011**, *83*, 823−840.
(16) Lo, K. K.-W.; Li, S. P.-Y.; Zhang, K. Y. *New J. Chem.* **2011**, *35*, 265−287.
(17) Guerchais, V.; Fillaut, J.-L. *Coord. Chem. Rev.* **2011**, *255*, 2448−2457.
(18) You, Y. *Curr. Opin. Chem. Biol.* **2013**, *17*, 699−707.
(19) You, Y.; Cho, S.; Nam, W. *Inorg. Chem.* **2014**, *53*, 1804−1815.
(20) Ru, J.-X.; Guan, L.-P.; Tang, X.-L.; Dou, W.; Yao, X.; Chen, W.-M.; Liu, Y.-M.; Zhang, G.-L.; Liu, W.-S.; Meng, Y.; Wang, C.-M. *Inorg. Chem.* **2014**, *53*, 11498−11506.
(21) Wang, Q.; Franz, K. J. *Inorg. Chem. Biol.* **2014**, 233−274.
(22) de Silva, A. P.; Gunaratne, H. Q. N.; Gunnlaugsson, T.; Huxley, A. J. M.; McCoy, C. P.; Rademacher, J. T.; Rice, T. E. *Chem. Rev.* **1997**, *97*, 1515−1566.
(23) Kavarnos, G. J.; Turro, N. J. *Chem. Rev.* **1986**, *86*, 401−449.
(24) Rehm, D.; Weller, A. *Isr. J. Chem.* **1970**, *8*, 259−271.
(25) Fahrni, C. J.; Yang, L.; VanDerveer, D. G. *J. Am. Chem. Soc.* **2003**, *125*, 3799−3812.
(26) Miura, T.; Urano, Y.; Tanaka, K.; Nagano, T.; Ohkubo, K.; Fukuzumi, S. *J. Am. Chem. Soc.* **2003**, *125*, 8666−8671.
(27) Suppan, P. *J. Chem. Soc., Faraday Trans. 1* **1986**, *82*, 509−511.
(28) Weller, A. *Pure Appl. Chem.* **1968**, *16*, 115−123.
(29) Closs, G. L.; Miller, J. R. *Science* **1988**, *240*, 440−447.
(30) You, Y.; Cho, S.; Nam, W. *Inorg. Chem.* **2014**, *53*, 1804−1815.
(31) Xu, Z.; Baek, K.-H.; Kim, H. N.; Cui, J.; Qian, X.; Spring, D. R.; Shin, I.; Yoon, J. *J. Am. Chem. Soc.* **2010**, *132*, 601−610.
(32) Sumiya, S.; Shiraishi, Y.; Hirai, T. *J. Phys. Chem. A* **2013**, *117*, 1474−1482.
(33) Lee, P.-K.; Liu, H.-W.; Yiu, S.-M.; Louie, M.-W.; Lo, K. K.-W. *Dalton Trans.* **2011**, *40*, 2180−2189.
(34) Mataga, N.; Kaifu, Y.; Koizumi, M. *Bull. Chem. Soc. Jpn.* **1956**, *29*, 465−470.
(35) Von Lippert, E. *Z. Electrochem.* **1957**, *61*, 962−975.
(36) Koide, Y.; Urano, Y.; Hanaoka, K.; Terai, T.; Nagano, T. *ACS Chem. Biol.* **2011**, *6*, 600−608.
(37) Lewis, F. D.; Burch, E. L. *J. Am. Chem. Soc.* **1994**, *116*, 1159−1160.
(38) Taki, M.; Wolford, J. L.; O'Halloran, T. V. *J. Am. Chem. Soc.* **2004**, *126*, 712−713.
(39) Yuasa, H.; Miyagawa, N.; Izumi, T.; Nakatani, M.; Izumi, M.; Hashimoto, H. *Org. Lett.* **2004**, *6*, 1489−1492.
(40) van Dongen, E. M. W. M.; Dekkers, L. M.; Spijker, K.; Meijer, E. W.; Klomp, L. W. J.; Merkx, M. *J. Am. Chem. Soc.* **2006**, *128*, 10754−10762.
(41) Park, S. Y.; Yoon, J. H.; Hong, C. S.; Souane, R.; Kim, J. S.; Matthews, S. E.; Vicens, J. *J. Org. Chem.* **2008**, *73*, 8212−8218.
(42) Zhang, X.-a.; Hayes, D.; Smith, S. J.; Friedle, S.; Lippard, S. J. *J. Am. Chem. Soc.* **2008**, *130*, 15788−15789.
(43) Xue, L.; Liu, Q.; Jiang, H. *Org. Lett.* **2009**, *11*, 3454−3457.
(44) Vinkenborg, J. L.; van Duijnhoven, S. M. J.; Merkx, M. *Chem. Commun.* **2011**, *47*, 11879−11881.
(45) Xue, L.; Li, G.; Liu, Q.; Wang, H.; Liu, C.; Ding, X.; He, S.; Jiang, H. *Inorg. Chem.* **2011**, *50*, 3680−3690.
(46) Ciupa, A.; Mahon, M. F.; De Bank, P. A.; Caggiano, L. *Org. Biomol. Chem.* **2012**, *10*, 8753−8757.
(47) Li, M.; Lu, H.-Y.; Liu, R.-L.; Chen, J.-D.; Chen, C.-F. *J. Org. Chem.* **2012**, *77*, 3670−3673.
(48) Xue, L.; Li, G.; Yu, C.; Jiang, H. *Chem. - Eur. J.* **2012**, *18*, 1050−1054.
(49) Mikata, Y.; Sato, Y.; Takeuchi, S.; Kuroda, Y.; Konno, H.; Iwatsuki, S. *Dalton Trans.* **2013**, *42*, 9688−9698.
(50) Song, E. J.; Kang, J.; You, G. R.; Park, G. J.; Kim, Y.; Kim, S.-J.; Kim, C.; Harrison, R. G. *Dalton Trans.* **2013**, *42*, 15514−15520.
(51) Zhang, L.-K.; Wu, G.-F.; Zhang, Y.; Tian, Y.-C.; Tong, Q.-X.; Li, D. *RSC Adv.* **2013**, *3*, 21409−21412.
(52) Choi, J. H.; Ryu, J. Y.; Park, Y. J.; Begum, H.; Park, H.-R.; Cho, H. J.; Kim, Y.; Lee, J. *Inorg. Chem. Commun.* **2014**, *50*, 24−27.
(53) Gogoi, A.; Samanta, S.; Das, G. *Sens. Actuators, B* **2014**, *202*, 788−794.
(54) Yao, P.-S.; Liu, Z.; Ge, J.-Z.; Chen, Y.; Cao, Q.-Y. *Dalton Trans.* **2015**, *44*, 7470−7476.
(55) Similar dual emission behavior has been also observed for biscyclometalated Ir(III) complexes having 1,10-phenanthroline ligand (ref 1).
(56) Qin, Y.; Miranda, J. G.; Stoddard, C. I.; Dean, K. M.; Galati, D. F.; Palmer, A. E. *ACS Chem. Biol.* **2013**, *8*, 2366−2371.
(57) Li, S. P.-Y.; Lau, C. T.-S.; Louie, M.-W.; Lam, Y.-W.; Cheng, S. H.; Lo, K. K.-W. *Biomaterials* **2013**, *34*, 7519−7532.
(58) Adarsh, N.; Avirah, R. R.; Ramaiah, D. *Org. Lett.* **2010**, *12*, 5720−5723.
(59) Aubry, J.-M.; Pierlot, C.; Rigaudy, J.; Schmidt, R. *Acc. Chem. Res.* **2003**, *36*, 668−675.
(60) Nonoyama, M. *Bull. Chem. Soc. Jpn.* **1974**, *47*, 767−768.
(61) You, Y.; Han, Y.; Lee, Y.-M.; Park, S. Y.; Nam, W.; Lippard, S. J. *J. Am. Chem. Soc.* **2011**, *133*, 11488−11491.

DOI: 10.1021/acs.inorgchem.5b00967
Inorg. Chem. 2015, 54, 9704−9714